MATERIALS CHEMISTRY
FRONTIERS

RESEARCH ARTICLE

View Article Online
View Journal

Cite this: DOI: 10.1039/d5qm00902b

Supramolecular engineering of non-planar bridged-ethers: blue to red emission tuning and solution-processed OLED fabrication

Shouvik Bhuin, [ab] Upasana Deori, [b] Pandiyan Sivasakthi, [a] Avanigadda Madhu Niharika,[a] Pralok K. Samanta, [a] Pachaiyappan Rajamalli *[b] and Manab Chakravarty *[a]

There is an exigent demand for establishing a systematic supramolecular engineering strategy to support the extraordinary tuning of desired emission from functional fluorescent organic materials. Simultaneous emission modulation in solids, aggregates, solvents, and viscous media is highly onerous with several associated photophysical pitfalls. The present research has coined a design concept in which bridged oxo/thioethers are conjugated to a highly twisted molecular core, generating multisite nonplanarity within the molecular system. Moreover, the non-covalent interactions and slip-stack angles can be altered by reducing or expanding the heterocycle. Furthermore, alterations to the present heteroatoms result in various molecular packing patterns, including H, herringbone-H*, X, and charge-transfer (CT)-mediated J-type examples. In addition, the fluorophore's polarizability, electronic conjugation, and conformation can be systematically regulated to tune a wide range of emission, from blue to red. Indeed, we achieved a 118-nm emission tuning in solids, 150-nm emission modulation in aggregates, and 100-nm emission alteration in a viscous medium. Moreover, a 99-nm to 150-nm solvatochromic shift was attained for some fluorophores. Different emissions from aggregates and the viscous medium were also detected, and excimer formation was possible for some fluorophores, particularly in aggregates. Also, a noncytotoxic orange-red-emitting fluorophore was applied in solution-processed yellow OLED (organic light-emitting device) fabrication to realize its further utility.

Received 19th December 2025,
Accepted 27th February 2026

DOI: 10.1039/d5qm00902b

rsc.li/frontiers-materials

1. Introduction

Supramolecular modification is highly entrancing in relation to organic fluorescent materials and has become a potential strategy to achieve omnipresent emission in solids and solutions. Even though this omnipresent emission in solids, solutions, aggregates, and viscous media is alluring, it often faces formidable challenges due to mutually exclusive photophysical principles.[1,2] Nevertheless, omnipresent emission from a fluorophore strongly suggests it could have various roles for optoelectronic and biological applications.[3,4] Over time, reports featuring solid- and solution-state emitting fluorophores have seemed incremental, although some noteworthy modular design concepts were established earlier to allow emission tuning in solids and solutions.[5] For instance, by attaching flexible alkyl chains to 7-diphenyl-benzo[1,2,5]thiadiazole-based conjugates, the closely packed molecular architecture could effectively be isolated to suppress π–π stacking, resulting in strong emission in aggregates and solvents.[6] Moreover, an anthracene and phenothiazine/triphenylamine-based twisted asymmetrical molecular framework with a supple alkyl chain could offer enhanced rigidity in a dense medium to create radiative relaxation, leading to the display of bright emission in solids, aggregation- and viscosity-induced blueshifted emission, and notable solvatochromism due to the favorable outputs of several quantum chemical descriptors.[7] 'V'-shaped herringbone packing originating from an anthracene-indole-based multisite-twisted fluorophore, with all its molecular parts aligning on different planes, turned out to be a highly desirable design for emission enhancement in aggregates, and it showed mechano/acidofluorochromism in the solid state.[8] Excited-state conformational planarization with a reduced dihedral angle between the donor and acceptor of a triphenylamine and benzoindolone-based system earlier offered brilliant solid- and solution-state emission.[9] Also, the complementary flexibility and symmetry of benzotriazole-based molecules could produce a highly twisted structure with strong emission in the solid state and solvents due to the reorientable

[a] Department of Chemistry, BITS-Pilani Hyderabad Campus, Hyderabad-500078, India. E-mail: manab@hyderabad.bits-pilani.ac.in
[b] Materials Research Centre (MRC), Indian Institute of Science (IISc), Bangalore 560012, India

and polarizable components of the molecular architecture.[10] Lately, fluorophores containing bridged oxo- and thioethers[11] or halogenated bridged ethers[12] have garnered ardent attention due to the scope of their supramolecular modulation, furnishing emission tuning. By introducing heteroatoms into their apparently planar systems, numerous crystal packing and non-covalent interactions could be generated to produce promising emitters. Indeed, these fluorophores experienced suitable deviations in planarity, especially at the junction of the heteroatom(s), relinquishing π–π stacking. Moreover, appropriate electronic and charge distributions, as well as excited-state planarity, root mean square displacement (RMSD), and reorganization energy, allowed them to exhibit strong emission in solvents as well.[11–13] While those reports have been inspiring, small but highly twisted molecules with bridged oxo/thioethers have rarely been reported to date, especially where emission tuning is possible in solids, solvents, aggregates, and viscous media simultaneously, involving a common strategy that can be applied to the basic molecular structure.

In our present work, we have conjugated a bridged oxo/thioether-based heterocyclic part with a naphthalene and dicyano-substituted ethylene moiety to play with the planarity at different sites of the resulting molecular system (Fig. 1). Hence, naphthalene and dicyano-substituted vinylene become the common scaffolds for all the designed probes. However, the heterocyclic part and the naphthalene component form a certain dihedral angle that can be varied with the alteration of the existing heteroatom(s) and the ring size of the heterocycle. Replacing the present heteroatom also modulates the planarity of the heterocyclic part. Thus, the overall molecular system becomes nonplanar at multiple sites; herein, we report a new class of five different fluorophores: **DBFNCN**, **DBTNCN**, **OXNCN**, **PONCN**, and **TANCN**.

Earlier, **OXNCN** was identified as a potent lipid droplet-targeted bioimaging probe for cancer cell discrimination,[14] but the properties of the remaining fluorophores were not investigated in detail. Meanwhile, this thoughtful design resulted in excellent supramolecular modulation, enabling significant emission control simultaneously in solids, solvents, aggregates, and viscous media, and, to the best of our knowledge, possibly for the first time for any vinylene-type fluorophore. In solids, alterations in heteroatom types and ring sizes resulted in different types of possible crystal packing, with variations in non-covalent interactions and slip-stack angles. In solvents, changes in heteroatom(s) and ring size again culminated in various possibilities regarding the extent of excited-state planarity relaxation, the HOMO–LUMO distribution, the natural transition orbital (NTO) contribution, the RMSD from the S_0 to S_1 state, and emission oscillator strength. Moreover, different types of aggregates were formed to afford tunable aggregation-induced emission (AIE) from these fluorophores. For all of them, the AIE effect was observed to be very close to their solid-state emission. However, their viscosity responsiveness again was different based on the present heteroatom and the ring size of the heterocyclic part. Surprisingly, in most cases, the viscosity-induced emission (VIE) was found to be different from the AIE effect. This clearly indicates that the AIE mechanism may not resemble the VIE mechanism in certain exceptional

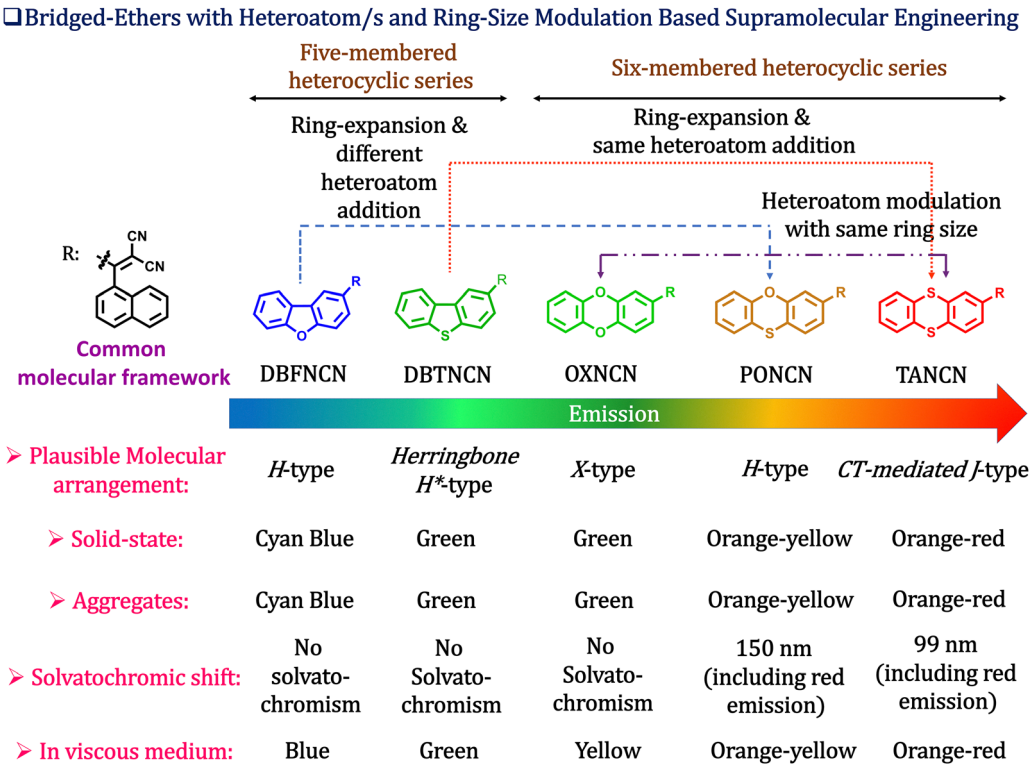

Fig. 1 An outline of the present work on supramolecular engineering resulting in emission tuning.

cases, which are reported herein. In fact, heteroatom replacement and ring-size variation led to varying extents of suppression of twisted intramolecular charge transfer (TICT) through aggregate formation. However, in a viscous medium, nonplanar architecture led to planarity-induced charge transfer (PICT) in the excited state, resulting in competition between TICT and PICT. This could further tune the VIE emission by adjusting the dihedral angle between the heterocyclic core and the vinylenyl naphthalene unit. All these observed photophysical phenomena were analyzed and explained through single-crystal analysis, DFT/TD-DFT calculations, and relevant and supporting scientific experiments.

To realize a real-world application, **TANCN** was utilized in the solution-processed fabrication of OLEDs. It is worth noting that **TANCN** is non-cytotoxic and exhibits orange-red emission, making it a suitable choice for OLED fabrication.

2. Results and discussion

2.1. Molecular engineering and synthesis

The designed molecules have a heterocyclic part and a naphthalene component, connected to a strong electron-withdrawing 'dicyano' core through a π-spacer (Fig. 2). The heterocyclic scaffolds are chosen with various heteroatom(s) (mainly S or O) replacements, offering a modular bridged ether system with controlled ring planarity, polarizability alterations, and variations in electronic distribution and orbital contributions.

The peripheral naphthalene was incorporated to induce torsion with the heterocycle, further promoting a nonplanar, multisite-twisted system. This would be crucial for creating different molecular conformations with various dihedral angles and for controlling emission profiles. Thus, the combined effect would produce different slip angles and crystal packing through various non-covalent interactions, thereby modulating the supramolecular structure. In addition, the twisted conformation may enable various molecular arrangements, disrupting π–π stacking interactions and promoting bright emission in the aggregated state.[8] Viscosity-sensitive emission is also anticipated from such twisted structures due to the restricted molecular motion with suitable dihedral angles between the heterocyclic and naphthalene cores, accompanying PICT in the motion-restricted state.[7,14] The D–π–A architecture, with strong –CN acceptors with a tilted conformation, facilitates pronounced ICT (intramolecular charge transfer) in solvents. The overall twisted structure can allow a switch from a less planar to a more planar conformation in the respective excited states in solvents of different polarities.[7,9] Furthermore, heteroatom replacement would alter crucial quantum chemical descriptors, such as RMSD (root mean square displacement), emission oscillator strength (f_{em}), the HOMO–LUMO energy gap, and the NTO (natural transition orbital) distributions, thereby affecting the emission wavelength and efficiency.[11,12]

As reported earlier, these dicyanoethylene compounds are synthesized using a unique strategy that starts from organophosphate-mediated three-step reaction pathways.[14] The related synthesis scheme (Fig. S1) and characterization details are presented in the SI.

2.2. Photophysical properties

2.2.1. Solid-state emission tuning. Steady-state photophysical experiments revealed that the absorption band of **PONCN** at λ_{max} = 530 nm was almost at a similar position to that of **TANCN** (λ_{max} = 533 nm) (Fig. S2). However, the corresponding emission of **PONCN** appeared at λ_{max} = 570 nm (orange-yellow) with an emission quantum yield Φ_f (%) = 3.00, while **TANCN** emitted at a near-red wavelength (λ_{max} = 593 nm) with enhanced emission efficacy [Φ_f (%) = 9.60] (Fig. 3 and Table 1). A different outcome was noticed for **OXNCN**, which displayed blue-shifted absorbance (λ_{max} = 465 nm) (Fig. S2) and emission (λ_{max} = 507 nm) compared to **PONCN** and **TANCN** (Fig. 3 and Table 1). To our great astonishment, Φ_f (%) in the solid state for the flattest oxanthrene-containing example, **OXNCN**, is notable for being the highest [Φ_f (%) = 10.22] among

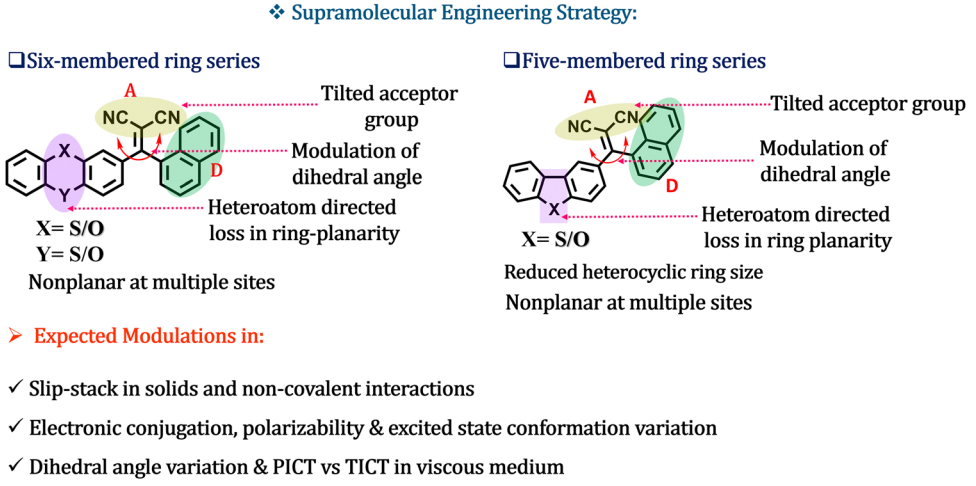

Fig. 2 The molecular engineering strategy to tune the emission profiles.

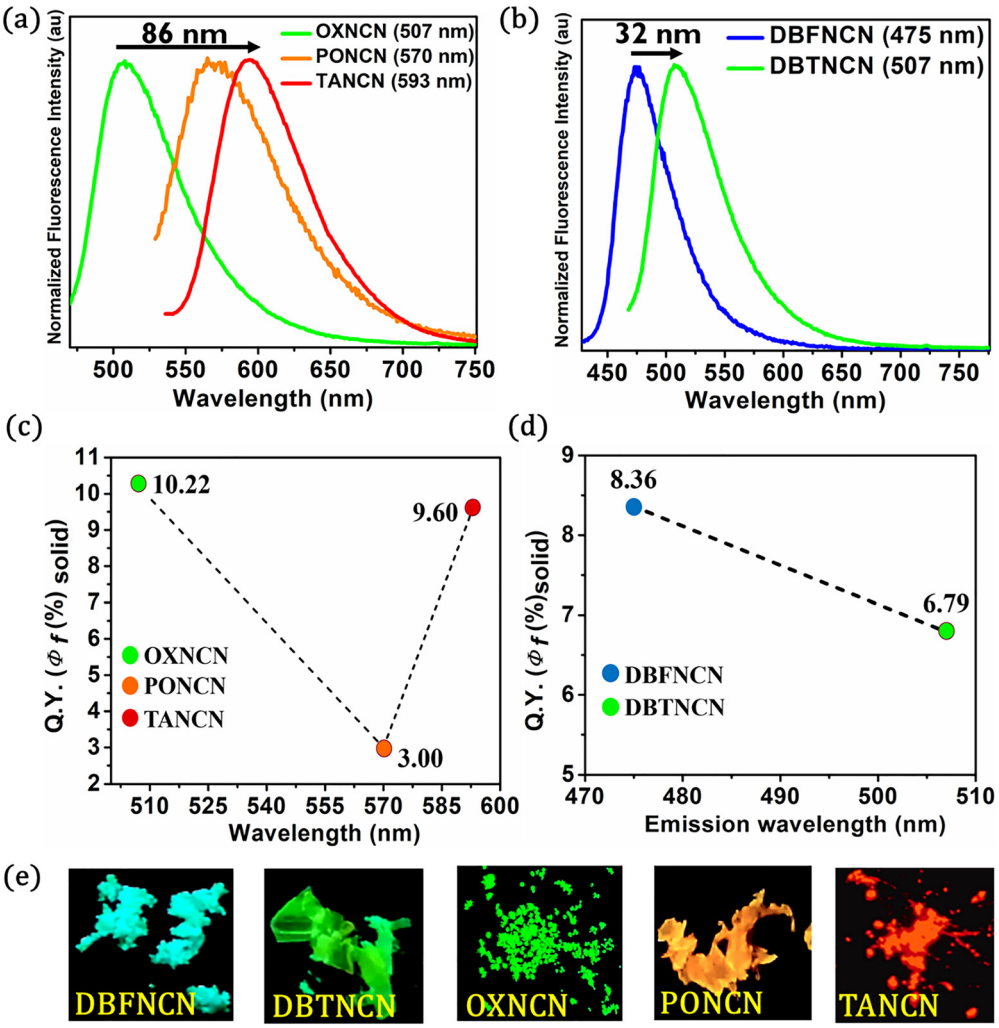

Fig. 3 Solid-state emission spectra for (a) the six-membered-ring series [λ_{ex} (nm): **OXNCN**: 465; **PONCN**: 530; **TANCN**: 533] and (b) five-membered-ring series [λ_{ex} (nm): **DBFNCN**: 425; **DBTNCN**: 461]; quantum yield variations with respective emission wavelengths for (c) the six-membered-ring series and (d) five-membered-ring series; and (e) captured images of the respective compounds under a 365-nm lamp.

Table 1 Heteroatom-replacement-guided solid-state emission tuning

System	Heterocycle ring size	Present heteroatom/s	Absorbance maximum (nm) (λ_{abs})	Emission (nm) (λ_{em})	Φ_f (%)
DBFNCN	Five	O (one)	425	475	8.36
DBTNCN	Five	S (one)	461	507	6.79
OXNCN	Six	O (two)	465	507	10.22
PONCN	Six	S and O (one each)	530	570	3.00
TANCN	Six	S (two)	533	593	9.60

the six-membered heterocycle-containing compounds, although **PONCN** and **TANCN** contained folded heterocycles. Next, in the single-heteroatom-based five-membered heterocyclic systems, **DBTNCN** showed longer absorbance (λ_{max} = 461 nm) (Fig. S2) and emission (λ_{max} = 507 nm) wavelengths than **DBFNCN** (λ_{abs} = 425 nm, λ_{em} = 475 nm) (Fig. 3 and Table 1). The solid-state Φ_f (%) for **DBFNCN** (8.36) is superior to **DBTNCN** (6.79). Hence, the inclusion of an S atom or increasing the number of S atoms by replacing the O atom enabled a bathochromic emission shift, as noticed for both six-membered (86 nm, 507 → 593 nm) and five-membered analogs (32 nm; 475 → 507 nm). However, incorporating or increasing the number of O atoms by replacing S would promote the solid-state emission efficiency in this newly designed system (Fig. 3 and Fig. S2 and Table 1).

For deeper insight into the observed photophysical outcomes, it was essential to analyze the molecular packing built *via* various noncovalent interactions. Single crystals of **TANCN**, **PONCN**, and **DBTNCN** were generated from a 3 : 1 $CHCl_3$: DMSO (dimethyl sulfoxide) solvent medium. Both **TANCN** and **PONCN** crystallized in a monoclinic $P12_1/n1$ space group

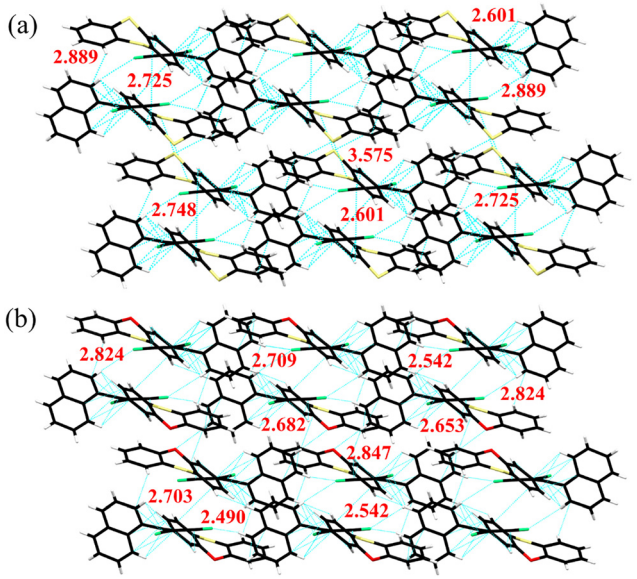

Fig. 4 The crystal packing of (a) **TANCN** and (b) **PONCN** (*b*-axis view); a few selected noncovalent interactions are presented with distances given in Å (atom colors: black, carbon; white, hydrogen; yellow, sulfur; red, oxygen; green, nitrogen).

with similar lattice parameters (Table S1 and Fig. 4a and b and Fig. S3 and S4). Apparently similar crystal packing patterns were observed for both **TANCN** and **PONCN**, characterized by alternative and translated parallel head-to-tail molecular rows (Fig. 4) involving various (∼21–22) noncovalent interactions (Table S2). Fig. 4a and b show that intermolecular S···S interactions (∼3.575 Å) between two thianthrene units of **TANCN** were prominent.

In addition, these twisted dimeric packing structures are again extended *via* C···H π-interactions of various distances (∼2.507–2.889 Å) to construct almost uniform rows (Fig. 4a and b). Unlike **PONCN**, the S atoms in **TANCN** contributed significantly to forming S···H and S···S interactions (Table S2). We observed that, with an offset face-to-face slip with respect to the naphthalene ring centroids (Fig. 5c and f), the molecular rows are again gradually translated, as depicted by the red rectangular shapes in Fig. 5a and d. **PONCN** has a smaller slip angle (54.70°, Fig. 5d–f) than **TANCN** (57.95°, Fig. 5a–c) because the molecular rows of **TANCN** are more glided over another than those of **PONCN** (Fig. 5a and d). The angle between the S_0 state transition dipole moments of any two molecules from alternative rows in the **TANCN** crystal packing structure (Fig. 5b)

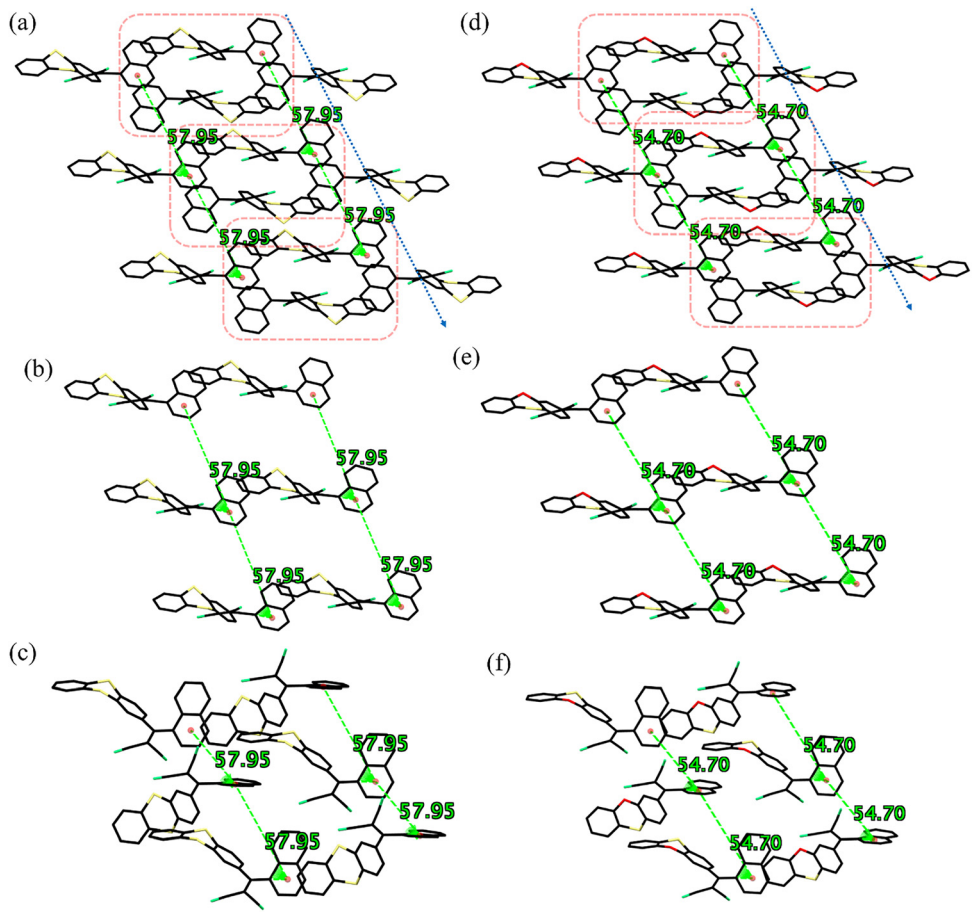

Fig. 5 Face-to-face slip with respect to the naphthalene-ring centroids with translated consecutive molecular rows (highlighted with the red rectangular shapes) with a *b*-axis view for (a) **TANCN** and (d) **PONCN**; alternative molecular rows with a *b*-axis view for (b) **TANCN** and (e) **PONCN**; and alternative molecular rows with an *a*-axis view to understand offset face-to-face slip for (c) **TANCN** and (f) **PONCN** [atom colors: black, carbon; white, hydrogen; yellow, sulfur; red, oxygen; green, nitrogen).

was calculated to be an obtuse angle 127.74° and so its supplementary angle is 52.46° (~54.70°), supporting the much closer presence of CT-mediated J-aggregates.[15,18] For **PONCN** (Fig. 5e), this calculated angle was 117.28° and hence, its supplementary angle was 62.72° (62.72° > 54.70°), implying an arrangement towards H-type compared with **TANCN** (Table S3). However, the CT-mediated J-arrangement or any similar phenomenon is really sporadic.[16–19] Centroid-to-centroid slip angle[20,21] and offset face-to-face stacking have been explored in earlier reports.[22,23] However, this CT-mediated J-packing caused **TANCN** to display a bathochromic shift increase of 23 nm (Fig. 3) with much better emission efficacy than **PONCN**, with dim orange-yellow emission (Fig. 3), while the absorbance (533 nm) was very close to the absorbance of **PONCN** (530 nm) (Fig. S2).

The high polarizability of the S atom and the nonplanar twisted molecular structure could explain the higher quantum yield for **TANCN**. The sp^3 unequal hybridization mode of the four lone pairs of electrons in the valence shell on two S atoms in **TANCN** can induce primitive repulsion.[24,25] Moreover, hanging peripheral benzene rings from the plane of the S atom restricts electron transfer and hampers coplanar packing, ultimately leading to intense emission. The crystal packing and the electron density map of **TANCN** also supported the same photophysical outcomes (Fig. S5). Various noncovalent interactions, such as H···H and O···H (Table S2), contributed to the poor quantum yield for **PONCN**. The calculated packing energy, considering the intermolecular potential and cluster energy data using Mercury 3.8,[26,27] of **PONCN**, was lower (−212.2 kJ mol^{-1}) than that of **TANCN** (−219.0 kJ mol^{-1}) (Tables S4 and S5). Thus, the stable crystal packing of **TANCN** would reduce the reorganization energy and facilitate a superior molecular arrangement, leading to redshifted emission. The inter-ring break for **TANCN** with J-type packing might favor the stability of a twisted fluorophore, and the polarizability of S atoms may create a higher dipole moment that can result in a zwitterionic state. Then, negative coulombic coupling or the repulsive nature of coulomb interactions might further assist **TANCN** in improving emission efficacy.

For **OXNCN**, atom replacement from S to O caused a significant 86-nm blue shift in emission and a 65–nm shift in absorption compared with solid **TANCN** (Fig. 3 and Fig. S2 and Table 1). Notably, the S_0 state optimized structures and the torsional angles of **TANCN** and **PONCN** were observed to be almost the same as their experimentally determined crystal structures (Fig. S6), and thus, we can rely on the optimized structure of **OXNCN** (Fig. S7 and S8) for subsequent conformation-based analysis. The S_0 state optimized structure and torsional angle between the heterocycle (h) and naphthalene (n), θ_{h-n}, in **OXNCN** were closer to **PONCN** than **TANCN** (Fig. S6–S8), nullifying the possibility of a *J*-type arrangement. It is surprising how **OXNCN** could avoid π···π stacking, despite having the flattest oxanthrene ring among all other heterocyclic analogs, and display the brightest solid-state emission. Moreover, TD-DFT optimization studies revealed that **OXNCN** seemed to gain better planarity [∠C–O–C ≈ 118°, and θ_{h-n} = −158°] in the S_1 state than in the S_0 state [∠C–O–C ≈ 116°, and θ_{h-n} ≈ −146°] (Fig. S8 and Table S6). Also, the average lifetime (τ, ns) increased with the increase in quantum yield from **PONCN** (τ = 2.15) to **TANCN** (τ = 3.13) to **OXNCN** (τ = 3.20) (Fig. S9a–c and Table S8). With the increased planarity of the oxanthrene ring, the emission intensity is typically expected to decrease and have a broader spectral width if H-type packing prevails.[28–30] Surprisingly, this was not the case for **OXNCN**. In fact, the widening of the emission spectrum, quantum yield, and lifetime of **OXNCN** were similar to those of **TANCN**. For **TANCN**, avoiding π···π stacking was easy, as the thianthrene ring is highly distorted, but **OXNCN** too could reduce π···π stacking in solids to a large extent, where flat oxanthrene rings should be far apart from each other to gain the brightest emission. We therefore propose that **OXNCN** exhibits a certain degree of X-type packing.[30] Also, molecular cross-stacking is possible on the flat oxanthrene side, where molecular planes may remain parallel, whereas on the naphthalene side, a rotational angle around the stacking axis is present. Even molecular cross-stacking can also occur on the naphthalene side, allowing the oxanthrene rings to be far apart from each other in the crystal packing structure, thereby avoiding lone-pair repulsion. Conversely, the five-membered heterocyclic analog **DBTNCN** preferred end-to-end dimeric herringbone ordering with almost H*-type arrangements[18] of the dibenzothiophene ring centroids in consecutive rows with a ~ 90° slip angle (Fig. S10a and c, and S11), accompanying four types of π···π, seven types of C···H π, two types of N···H, and two types of S···H interactions; interestingly, no S···S interaction is present (Tables S1 and S7). The crystal structure of **DBFNCN** could not be refined satisfactorily; however, the structure still arguably provides valuable clues (Fig. S10b). It may have a probable centroid-to-centroid slip angle of ~77.21^0 (relatively close to 90°) with respect to the dibenzofuran rings of alternative rows (Fig. S10b and d), indicating H-type packing ($54.7^0 < 77.21^0 < 90^0$).[30] Repulsion between oxygen lone pairs might have compelled the dibenzofuran rings into a head-to-tail arrangement for two consecutive rows. H-type packing was earlier reported to be energetically less favored and to display the lowest intermolecular interaction energy strength, but the highest repulsive exchange interaction.[18] This can cause overall blueshifted emission for the compounds of the five-membered heterocyclic series as compared to the compounds from the six-membered heterocyclic series. For H-type packing, the ring centers may create voids during alignment, resulting in weaker intermolecular π···π interactions, increasing the emission efficiency. However, the average lifetimes for **DBFNCN** and **DBTNCN** were determined to be 2.99 ns and 0.42 ns, respectively, resulting in a higher Φ_f (%) value for **DBFNCN** (Fig. S9d and e and Table S8). The emission curves of almost all the compounds could be fitted with bi-exponential decay, while for **DBTNCN**, there was a tri-exponential fit (Fig. S9 and Table S8). However, no longer-lived component was apparent in the decay profiles to indicate the presence of delayed emission. Again, from TD-DFT calculations (Table S9), it was revealed that the energy gap between the singlet (S_1) and triplet (T_1) states (ΔE_{ST}) was ~0.7–0.9 eV for all compounds. Of note, any value of

$\Delta E_{ST} \leq 0.2$ eV is generally considered to be ideal for favorable reverse intersystem crossing (RISC) to display thermally activated delayed (TADF) emission.[31,32] Hence, the theoretically calculated data corroborated well with the experimental findings.

2.2.2. Solution-state emission tuning. While the absorption profile showed no considerable shift for **TANCN** (Fig. S12a), a 99-nm emission redshift was noticed in **TANCN** from hexane to dichloromethane (DCM), with negligible intensity in DMSO and *N,N*-dimethylformamide (DMF) (Fig. 6a and c). Conversely, along with a subtle switch in absorbance (Fig. S12b), **PONCN** exhibited a 150-nm bathochromic emission shift, retaining commendable emission even in DMSO and DMF (Fig. 6b and d). Variations in Stokes shift and Φ_f with varying solvent polarity were prominent for **TANCN** and **PONCN** (Fig. S13 and S14 and Table 2). **OXNCN** was emissive only in hexane [Φ_f (%) = 2.05] and 1,4-dioxane [Φ_f (%) = 1.66]. Its emission was extremely weak in polar DCM [Φ_f (%) = 0.16] and DMF [Φ_f (%) = 0.12] (Fig. S15), as we reported earlier.[14] The five-membered-ring containing analogs **DBTNCN** and **DBFNCN** did not exhibit bright emission in solvents, except for faint bluish fluorescence irrespective of the solvent polarity (Fig. S16 and S17).

For **TANCN**, the HOMO–LUMO energy gap (ΔE_{H-L}) reduced minutely from hexane (3.254 eV) to DCM (3.239 eV), indicating lower-energy emission in DCM (Fig. S18). Interestingly, for **PONCN**, the calculated ΔE_{H-L} values did not differ noticeably from hexane to DCM (Fig. S19). **TANCN** exhibited a 74% H−1 → L orbital contribution in hexane, while this was 92% in DCM. **PONCN** exhibited an 89% H → L orbital contribution in hexane, while this was 87% in DCM (Table S10). From NTO analysis, we found that the hole and electron NTOs were π and π* in nature, and in the S_1 state, there were 99.2% contributions from hNTO to eNTO for **TANCN** in both hexane and DCM solvents (Fig. S20). However, for **PONCN**, 98.8% of contributions were from hNTO to eNTO in hexane and DCM solvents (Fig. S21). This might be a reason for **PONCN**'s overall blueshifted emission compared to **TANCN**. Moreover, as a representative compound, we selected **PONCN** for a dihedral angle (θ_{h-n}) *vs.* emission scan in the S_1 state in hexane. From this theoretical calculation, we received the indication that at θ_{h-n} of ∼160°, **PONCN** may have blue emission (462 nm) in hexane, which was actually very near to the experimental value (485 nm) (Fig. S22). Again, in hexane, the excited state planarity relaxation at θ_{h-n} from S_0 to S_1 for **TANCN** is greater (∼145.81° → 159.74°) than that for **PONCN** (∼147.27° → 158.96°). Even in the S_1 state, ∠C–S–C is more twisted (∼102.33°) for **PONCN**, while for **TANCN**, both ∠C–S–C angles are more relaxed (∼107°) (Table 4). The greater extent of excited-state planarity relaxation caused a higher emission efficiency for **TANCN** than for **PONCN** in hexane, as we observed in our earlier research as well.[7,8] The same structural trend is also observed in DCM (Table 4), which may explain the difference in emission efficiencies of the two dyes in this solvent. Moreover, the presence of the S atom led to a conformational twist in the thianthrene or phenoxathiine ring, which is puckered yet maintains a certain degree of hindered conjugation and increased polarizability. As expected, the calculated polarization and dipole moment of **TANCN** were much higher in hexane and DCM than those of **PONCN** (Table 3). This high polarizability can influence electrostatic interactions and interaction energies, which in turn affect the excited-state conformation.[33] As shown in the NTOs for **PONCN** and **TANCN** in hexane and DCM (Fig. S20 and S21), the electron (eNTO) is mainly spread over the heterocyclic and dicyano parts, and partially on the naphthalene part, while the hole is concentrated on the heterocyclic and dicyano parts. The electron and hole distribution did not fully overlap on the heterocyclic and dicyano parts, indicating the CT character of the S_1 to S_0 transition, while moderate

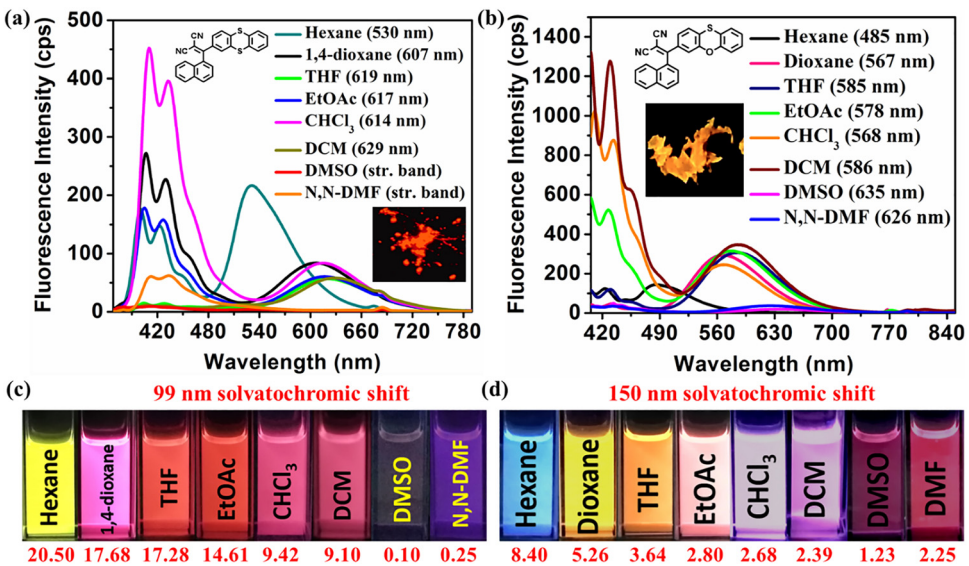

Fig. 6 Solution-state emission with solvatochromic shifts: (a and c) **TANCN** (10^{-5} M) and (b and d) **PONCN** (10^{-5} M); solid-state images are given in the insets, and all photos were taken under a 365-nm UV lamp; Φ_f (%) values in respective solvents are also stated below panels (c) and (d) (str. band: no specific emission peak except for some vibrational bands).

Table 2 Solvatochromic properties for **TANCN** and **PONCN**. The used probe concentration is 10^{-5} M. The solvatochromic shifts are specified for each solvent with respect to hexane. The maximum wavelength (nm) only is considered for all λ_{abs} and λ_{em} values

Compound	Solvent	E_T (30) (kcal mol^{-1})	λ_{abs} (nm)	λ_{em}, CT only (nm)	Stokes shift (cm^{-1})	Solvatochromic shift (nm)	Φ_f (%)
TANCN with λ_{em} (solid) = 593 nm	Hexane	31.0	341	530	10 457.59	0	20.50
	1,4-dioxane	36.0	342	607	12 765.30	77	17.68
	THF	37.4	340	619	13 256.68	89	17.28
	EtOAc	38.1	350	617	12 363.97	87	14.61
	$CHCl_3$	39.1	350	614	12 284.78	84	9.42
	DCM	40.7	348	629	12 837.38	99	9.10
	DMSO	45.1	343	strb	—	—	0.103
	DMF	43.2	342	strb	—	—	1.25
PONCN with λ_{em} (solid) = 570 nm	Hexane	31.0	386	485	5288.18	0	8.40
	1,4-dioxane	36.0	387	567	8203.11	82	5.26
	THF	37.4	387	585	8745.78	100	3.64
	EtOAc	38.1	388	578	8472.16	93	2.80
	$CHCl_3$	39.1	388	568	8167.56	83	2.68
	DCM	40.7	390	586	8576.18	101	2.39
	DMSO	45.1	392	635	9762.17	150	1.23
	DMF	43.2	412	626	8297.40	141	2.25

Table 3 The calculated results for the total dipole moment and total polarization in two different solvents (using the M06-2X/6-31G(d) level of theory)

	S_1			
	DCM		Hexane	
Molecule	Total polarization (au)	Total dipole moment (Debye)	Total polarization (au)	Total dipole moment (Debye)
PONCN	449.138	9.682	375.604	8.114
TANCN	471.913	9.902	394.531	8.274
	S_0			
	DCM		Hexane	
Molecule	Total polarization (au)	Total dipole moment (Debye)	Total polarization (au)	Total dipole moment (Debye)
PONCN	399.784	7.454	344.499	6.636
TANCN	420.629	7.383	361.347	6.606

overlap is also present to indicate the presence of LE character as well, along with CT.[34,35] For both **PONCN** and **TANCN** in hexane and DCM, an overall significant change in dipole moment from the S_0 (~6.6–7.5 D) to the S_1 state (~8.1–9.9 D) was noticed (Table 3). This further implied the existence of a CT transition.[34] Conversely, even in the S_1 state, the lower value of the calculated dipole moment (~8.1–9.9 D) dilutes the probability of an HLCT transition, as HLCT is often associated with a larger dipole moment value (~12–18 D).[34] Meanwhile, for both **TANCN** and **PONCN**, apart from emission at ~520 nm, emission with vibrational structured bands at ~420–450 nm was observed due to the naphthalene core, resulting in mixed emission with different shades of color (Fig. 6). Conversely, in DMSO, despite excited state planarity relaxation, the calculated emission oscillator strength (f_{em}) for **TANCN** was ~0.3994, while for **PONCN** it was ~0.5718, a much higher value. The RMSD for **TANCN** in DMSO was higher (~0.5706 Å) than for **PONCN**, where it was ~ 0.4328 Å. The same trend was observed in *N*,*N*-dimethylformamide (DMF). A higher emission oscillator strength and lower RMSD could contribute to improved emission efficacy for **PONCN** in polar solvents such as DMSO and DMF (Fig. 6).[7]

For **OXNCN**, we noticed structured spectra with existing LE state emission and CT emission at comparatively longer wavelengths (Fig. S15). CT could have been generated due to a well-separated HOMO and LUMO (Table S11), while the redshifted weak emission in polar solvents might be due to reduced ΔE_{HL}. TD-DFT analysis revealed that the acquired planarity based on the ∠C–O–C angle from S_0 to S_1 was comparable between a nonpolar and polar solvent (Table 4). However, the gained excited-state planarity at θ_{h-n} (the torsion angle between oxanthrene and naphthalene) for **OXNCN** was inferior in a nonpolar solvent compared with polar solvents (Table 4, Fig. S23). Furthermore, it might have opened up a TICT state with larger planarity relaxation at θ_{h-n} from S_0 to S_1 to diminish its emission.[14]

For **DBTNCN**, the HOMO–LUMO energy gap reduced gradually from hexane (~3.5 eV) to *N*,*N*-DMF (~3.46 eV) with a 99.7% contribution from hNTO to eNTO in hexane, while this was 99.9% in DMF. The S_1-state ∠C–S–C for **DBTNCN** was ~90° in both solvents, but in DMF, **DBTNCN** experienced a loss of planarity at θ_{h-n} in the S_1 state compared to that in the S_0 state (Table 4), making it almost non-emissive (Fig. S16). For **DBFNCN**, the HOMO–LUMO energy gap reduced gradually from hexane (~3.63 eV) to *N*,*N*-DMF (~3.52 eV), with a 99.7% contribution from *h*NTO to *e*NTO in hexane, while this was 99.9% in DMF. The S_1-state ∠C–O–C for **DBFNCN** was ~106° in both solvents, but in DMF, **DBFNCN** experienced almost no gain in planarity at θ_{h-n} in the S_1 state compared to that in the S_0 state, making it almost non-emissive (Table 4 and Fig. S17).

Solution-state time-resolved spectroscopy discloses the lifetimes of **TANCN**, **PONCN**, and **OXNCN** in nanoseconds (ns), without the presence of any delayed component (Fig. S24 and

Table 4 TD-DFT-calculated bond angles for heteroatomic centers and torsion angles (θ_{h-n}) between heterocycles and tilted naphthalene (all in °) in different solvents (using the B3LYP/6-31g(d) level of theory)

Compound	Solvent	S_0 ∠C–S–C	S_1 ∠C–S–C	S_0 ∠C–O–C	S_1 ∠C–O–C	θ_{h-n} (S_0)	θ_{h-n} (S_1)
TANCN	Hexane	101.69	107.46	—	—	−145.81	−159.74
		101.27	107.50				
	DCM	101.75	107.77	—	—	−145.11	−160.60
		101.31	107.53				
	DMSO	100.69	107.87	—	—	−143.97	−160.93
		100.33	107.59				
	DMF	101.75	107.86	—	—	−144.94	−160.89
		101.31	107.59				
PONCN	Hexane	98.85	102.33	119.38	124.55	−147.27	−158.96
	DCM	98.93	102.41	119.41	124.50	−146.47	−160.62
	DMSO	97.98	102.43	117.86	124.48	−145.37	−161.06
	DMF	98.95	102.43	119.42	124.48	−146.26	−161.03
OXNCN	Hexane	—	—	116.67	118.42	−148.20	−158.45
				116.56	118.55		
	DCM			116.74	118.65	−147.78	−159.47
				116.57	118.51		
	DMF			116.76	118.72	−147.75	−159.83
				116.57	118.50		
DBTNCN	Hexane	91.03	90.91	—	—	147.09	153.09
	DMF	90.91	90.95	—	—	153.09	146.95
DBFNCN	Hexane			106.08	106.03	−146.59	−149.48
	DMF			106.13	106.13	−145.19	−145.30

Table S12). With increasing solvent polarity, the quantum yields reduced, whereas the respective average lifetime values increased. Strong ICT with a huge amount of excited-state geometry relaxation could encourage a non-radiative decay pathway, forming a TICT to decrease the emission efficiency, while the formation of a comparably longer-lived relaxed state simultaneously could increase the overall average lifetime. However, the calculated ΔE_{ST} values for all the compounds in the respective solvents were observed to be too large to allow the possibility of TADF emission (Table S12).[32]

2.2.3. Aggregation-induced emission (AIE). Aggregation-induced emission (AIE) defines a photophysical phenomenon where nonfluorescent[36] or weakly emissive compounds display bright emission or enhanced emission[4,7] in an aggregated state, and this can be realized in several real-world applications.[4,7,8,14] From the absorbance spectra, it was understood that upon aggregation with an increasing water fraction, f_w (%, *v*/*v* in MeCN/water), from 0 to 99% at a probe concentration of 10^{-5} M, there was an absorbance redshift of 57 nm for **TANCN**, 33 nm for **PONCN**, and 18 nm for **OXNCN** (Fig. S25). Similar AIE studies of the five-membered compounds showed a comparable absorbance redshift of 35 nm for **DBTNCN** and 20 nm for **DBFNCN** (Fig. S25). This trend in absorbance shift was also applicable to higher probe concentrations. Hence, the tendency for J-type aggregate formation follows the order of **OXNCN** < **PONCN** < **TANCN** and **DBFNCN** < **DBTNCN**. For **TANCN**, upon aggregation, the 57-nm redshifted absorbance and emission at ~600 nm could be attributed to the formation of CT-mediated J-aggregates (Fig. S25 and S26). The aggregation state is different from the solid state, with random and non-directional supramolecular interactions; however, it tends to reach a solid state.[28] Notably, the AIE emission was closer to the respective solid-state emission (Table 5), and hence, similar molecular packing is anticipated in both the aggregate and solid states. As indicated by the **TANCN** crystal structure analysis, the presence of S···S interactions in aggregates may help **TANCN** organize its head-to-tail molecular rows with a slip angle, which could be greater than 54.7°. In the excited state, θ_{h-n} (S_1) can become more planar to increase conjugation between the donor and acceptor moieties, which would be beneficial for the formation of CT-mediated J-aggregates.[15] At higher probe concentrations, excimer emission takes precedence over monomeric emission (Fig. S26). In excimers, coplanar stacking would be hampered by the twisted structures, while the high polarizability of the S atoms may lead to the formation of zwitterionic dimers with high dipole moments. This may further help counterbalance electrostatic repulsion to enhance emission.[37] Thus, the high value of F/F_0 at a probe concentration of 10^{-4} M for **TANCN** can be

Table 5 Parameters related to aggregation-induced emission for the synthesized compounds and a comparison with solid-state emission wavelengths

Compound	Solid-state emission (nm)	Absorbance redshift (nm) in the aggregated state (10^{-5} M)	Emission (nm) at a higher probe concentration (10^{-4} M)	Emission (nm) at a lower probe concentration (10^{-5} M)	F/F_0 (10^{-4} M)	F/F_0 (10^{-5} M)	Type of aggregate anticipated
DBFNCN	475	20	475	465	~1.1	~0.2	H
DBTNCN	507	35	493	493	~18	~6	H*
OXNCN	507	18	523	517	~45	~20	probable X
PONCN	570	33	587	587	~7.2	~6.6	H-type
TANCN	593	57	600	596	~120	~30	CT-mediated J

justified. Moderately redshifted absorbance of 33 nm upon aggregation indicated the lower tendency of **PONCN** to adopt a J-arrangement (Fig. S25 and S27 and Table 5). Interestingly, **PONCN** displayed comparably weaker AIE emission at both concentrations (Fig. S27). This could be possible if **PONCN** experienced a greater tendency towards an H-type arrangement compared to **TANCN** in aggregates. Due to the presence of the O atom in phenoxathiin, multiple van der Waals and O···H interactions in **PONCN** aggregates may help them to exhibit moderate AIE features despite the highly nonplanar conformation. **OXNCN** displayed a third of the redshift in absorbance (18 nm) compared to **TANCN** (57 nm) (Fig. S25 and Table 5), which implied that the molecular arrangement could never be J-type. On the contrary, H-aggregates usually exhibit weaker emission with a wide spectrum.[18,30] Notably, oxanthrene is the flattest six-membered heterocycle discussed herein, yet still **OXNCN** displayed strong AIE emission at both concentrations. The F/F_0 value of **OXNCN** was almost similar to the F/F_0 value of **TANCN** at a concentration of 10^{-5} M (Table 5 and Fig. S26 and S28). Hence, the AIE strength of **OXNCN** did not vary much with changing probe concentration. For both concentrations of **OXNCN**, the decay profile could be fitted in a triexponential manner, where the two long-lived components had shorter lifetimes (1.36 and 2.72 ns at 10^{-4} M; 1.38 and 2.76 ns at 10^{-5} M), but one short-lived component had a high lifetime (5.43 ns at 10^{-4} M; 5.52 ns at 10^{-5} M).[14] We expect that **OXNCN** might adopt an X-type arrangement to some extent. The lone pairs of oxygen will create repulsion, causing the oxanthrene rings to move away from each other during molecular cross-stacking in possible X-aggregates, thereby enhancing the AIE emission. The existing torsion angle between the oxanthrene and naphthalene parts would further assist in diminishing the harmful π···π stacking during aggregation.[14] For **DBTNCN**, herringbone H*-type packing was found during single-crystal analysis. The slightly blueshifted emission of **DBTNCN** aggregates (Fig. S29) could be attributed to any associated reorganization energy that contributed to stability in the possible herringbone packing, with restricted structural relaxation.[38] For **DBFNCN**, the AIE effect at lower probe concentrations was almost negligible. This anomaly was even noticed for our previously reported emitters, which were not AIE active.[39,40] However, a weak and wide emission profile was noticed at higher probe concentrations to indicate the formation of H-type aggregates (Fig. S30). At lower water fractions, the weak emission and the observed structural bands for most of the fluorophores (Fig. S26–S30) could be accounted for based on the existing dark TICT state and vibrational bands, which vanished upon aggregate formation at higher water fractions.

2.2.4. Viscosity-induced emission (VIE). Often, viscosity-induced emission (VIE) serves as proof of restricted intramolecular motion, which is considered the main cause of AIE. AIE and VIE are understood as almost the same phenomenon.[41] However, we noticed that a few of our synthesized compounds behaved differently in a viscous medium compared with their AIE properties.

Except for **OXNCN**, the absorbance shifts of the remaining fluorophores were negligible upon exposure to high-viscosity media compared to the absorbance shifts of their AIE features (Fig. S31 and Tables 5 and 6). At a lower probe concentration, **TANCN** showed no response to viscosity (Fig. S32 and Table 6), but exhibited considerable AIE features (Fig. S26 and Table 5). Again, at lower probe concentrations, **PONCN** and **OXNCN** exhibited moderate increases in their viscosity-induced emission (Fig. S33 and S34 and Table 6), while maintaining brighter AIE characteristics (Fig. S27 and S28 and Table 5). **OXNCN** displayed yellow emission (545 nm) in response to viscosity (Fig. S34 and Table 6), while it exhibited green AIE (517–523 nm) at both lower and higher concentrations (Fig. S28 and Table 5). The temperature dependence of **OXNCN** was also verified in PBS solution, as it contains a significant water fraction with higher viscosity; thus, in PBS, **OXNCN** should exhibit emission that combines AIE and VIE effects. Indeed, in PBS above 35 °C, **OXNCN** (10^{-5} M) displayed emission at around 530 nm with lower intensity; however, the efficiency of emission gradually increased with decreasing temperature (Fig. S35). This proves that the molecular motion of **OXNCN** was responsive to the changing viscosity of the neutral PBS buffer medium at different temperatures. Again, **DBFNCN** exhibited significantly blueshifted emission in the viscous medium at lower concentrations, but it displayed green emission at higher probe concentrations (Fig. S37 and Table 6). These findings strongly suggest that viscosity-responsive emission follows different mechanisms from the AIE characteristics. To emit brightly, fluorophores can restrict their intramolecular motion in a viscous medium when they are not even forming aggregates. In polar MeOH, they can experience dark TICT to quench their emission,[42] but in a highly viscous medium, accompanied by the restriction of intramolecular rotation (RIR), they can undergo favorable excited-state planarity relaxation to avoid TICT. This planarity relaxation may open up the PICT state. Unlike TICT, PICT is electronically allowed, as the participating orbitals largely overlap due to their parallel orientation during the transition.[42,43] Again, in a highly viscous

Table 6 Parameters related to viscosity-induced emission for the synthesized compounds and an emission wavelength comparison with AIE

Compound	AIE emission (nm) (10^{-4} M/10^{-5} M)	Absorbance redshift (nm) in a viscous medium (10^{-5} M)	Emission (nm) at a higher probe concentration (10^{-4} M)	Emission (nm) at a lower probe concentration (10^{-5} M)	F/F_0 (10^{-4} M)	F/F_0 (10^{-5} M)
DBFNCN	475/465	12	500 [f_g (%): ~90]	405 [f_g (%): ~99]	~13	Not considerable
DBTNCN	493/493	8	507 [f_g (%): ~90]	500 [f_g (%): ~90]	~22	~11
OXNCN	523/517	40	545 [f_g (%): ~90]	545 [f_g (%): ~90]	~14	~6
PONCN	587/587	13	578 [f_g (%): ~99]	582 [f_g (%): ~99]	~19	~3
TANCN	600/596	15	600 [f_g (%): ~90]	Not considerable	~95	Not considerable

medium, PICT offers a lower RMSD, higher emission oscillator strength, and higher transition energy to cause enhanced emission. For **TANCN**, fewer molecules prevailed at a lower probe concentration, and although intramolecular restriction of rotation and vibration could be achieved, intermolecular motion still could not be restricted. At a higher probe concentration of **TANCN**, more molecules probably could restrict intermolecular movement along with freezing intramolecular motion to emit very brightly. As aggregation was impossible or very weak, we expected that PICT could not overcome TICT completely, so that lower probe concentrations of **PONCN** and **OXNCN** would show moderate emission in a viscous medium. **DBTNCN** could respond to viscosity properly, and its VIE strength was comparable to its AIE features (Fig. S29 and S36). Possibly, its monomers could exhibit favorable excited state planarity at θ_{h-n} (S_1) with increased electronic conjugation. For **OXNCN** monomers, θ_{h-n} (S_1) possibly differed from θ_{h-n} (S_1) in aggregates to increase electronic conjugation, causing redshifted VIE as compared to AIE. The surprisingly blueshifted VIE for **DBFNCN** at a low concentration could indicate the existence of high reorganization energy. Overall, for all the fluorophores, the VIE characteristics were weaker than the emission in aggregates due to competing TICT, which markedly subdued the effects of PICT.

2.3 Application in small-molecule fluorophore-based organic light-emitting diode (OLED) fabrication

Donor–π–acceptor systems are highly celebrated for OLED fabrication.[44] **TANCN** had orange-red emission in the solid state (Fig. 3), and it was previously found to be noncytotoxic.[14] Hence, to explore the electroluminescence behavior of small-molecule **TANCN**, we have fabricated a solution-processed OLED device with the following optimized configuration: ITO (100 nm)/PEDOT:PSS (40 nm)/PVK (20 nm)/30 wt% **TANCN**:CBP (20 nm)/PPT (10 nm)/TmPyPB (50 nm)/Liq (2 nm)/Al (100 nm). Indium tin oxide (ITO) and aluminum (Al) were selected as the anode and cathode, respectively. Poly(3,4-ethylenedioxythiophene) polystyrene sulfonate (PEDOT:PSS) was used as the hole-injection layer, and polyvinylcarbazole (PVK) as the hole-transport layer. 1,3,5-Tri(m-pyrid-3-yl-phenyl)benzene (TmPyPB) and 8-hydroxyquinolinolato-lithium (Liq) were adopted as the electron transport layer and electron injection layer, respectively. 2,8-Bis(diphenylphosphoryl)-dibenzo[*b*,*d*]thiophene (PPT) served as an exciton-blocking layer to restrict carriers from recombining in the interface. 4,4′-Bis(*N*-carbazolyl)-1,1′-biphenyl (CBP) was selected as the host in the emissive layer (Fig. 7a and b and Fig. S38) due to its bipolar nature, facilitating balanced carrier transport. The **TANCN**-based OLED device exhibited luminance of 10 082 cd m^{-2} and a blue-shifted emission spectrum, with an electroluminescence peak at 555 nm. The maximum external quantum efficiency (EQE), power efficiency (PE), and current efficiency (CE) are 1.9%, 5.4 lm W^{-1} and 7.7 cd A^{-1}, respectively (Fig. 7c–e). Although the poor EQE may be attributable to the low PLQY of the emitter (~9%), the potential of the emitter for light-emitting applications has been demonstrated, indicating room for improvement through further optimization. Of note, in the OLED device, **TANCN** is dispersed in a host matrix that may suppress aggregation and π–π stacking, resulting in blue-shifted emission (Fig. S39) compared to the powder form.

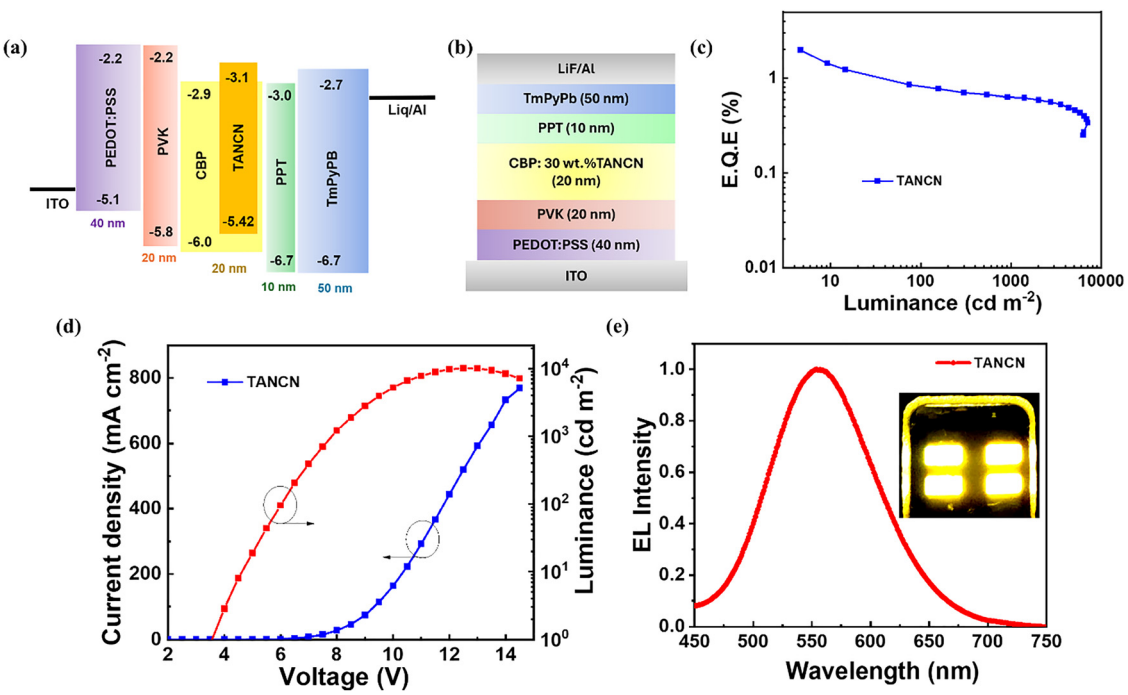

Fig. 7 (a) The energy level diagram, (b) device structure, (c) EQE *vs.* luminance plot, (d) current density-voltage-luminance plot, and (e) electroluminescence intensity *vs.* wavelength plot with a picture of the OLED device in the inset. The HOMO–LUMO energy levels for **TANCN** were determined using cyclic voltammetry experiments (Fig. S38).

Additionally, the influence of the multilayer stack can further blue-shift the EL emission (Fig. 7e). Such blue shifts relative to solid-state PL are commonly observed under electrical excitation and arise from these environmental differences.[45]

3. Conclusions

In short, the use of a twisted molecular core–conjugated non-planar bridged oxo- and thioethers was proven to be an outstanding design concept that allowed extraordinary emission tuning in solids, solvents, aggregates, and viscous media. This work is successful in prescribing a new design where we can predict the obtained emission logically. Importantly, we understood that introducing multiple S atoms into a six-membered heterocycle could generate S···S noncovalent interactions with a slip-stack angle greater than a key angle to nurture a CT-mediated J-arrangement. This culminated in bright redshifted emission in all situations, while the introduction of O atom(s) continuously blueshifted the emission in solids, aggregates, and a viscous medium. Moreover, X/H-type molecular arrangements were only favored in the presence of O atoms, irrespective of the ring size. Expanding the ring size with the same heteroatom could also redshift the emission in solids, aggregates, and viscous media. However, excited-state planarity relaxation greatly affected the emission strength in solution, accompanied by a polarizability effect and electronic conjugation. Moreover, it was realized that the presence of S atoms alone was not sufficient to obtain solvatochromism, but the ring size really did matter. However, the presence of O atoms alone could not result in solvatochromic shifts, irrespective of the ring size. Our findings also challenge the expectation that the same emission color will be obtained in aggregates and a viscous medium from a particular fluorophore. The dihedral angle and extent of favorable PICT could result in a different mechanism and bright emission in a viscous medium at a different wavelength from the AIE color. As an initial endeavor, noncytotoxic **TANCN** with orange-red emission in solids was implemented in the fabrication of a solution-processed yellow-emitting OLED. **TANCN** had a solid-state QY of almost 9%, and the EQE of the device still achieved almost up to 2%. While many small-molecule fluorophores quench in devices, **TANCN** could manage considerable luminance despite its moderate solid-state PLQY. In the future, we aim to work on the structures of twisted bridged ethers to achieve better efficiency with favorable emission tuning in solids and solutions and to achieve a brighter EQE in the fabricated OLED device.

Author contributions

S. B.: conceptualization, experiments, analysis, original manuscript - writing; U. D.: experiments and analysis; P. S.: theoretical studies; A. M. N.: help with conducting experiments; P. K. S.: supervision of the theoretical investigation; P. R.: supervision and facilities for OLED device fabrication; M. C.: supervision of the entire project, result analysis, draft corrections, lab facilities, and funding.

Conflicts of interest

There are no conflicts to declare.

Data availability

The data supporting this article have been included as part of the supplementary information (SI). This study was carried out using publicly available data that are discussed in the manuscript. All the spectra, molecular packing, theoretical data and all the relevant information are included in SI. The data analysis scripts for this article are available in the SI. See DOI: **https://doi.org/10.1039/d5qm00902b**.

CCDC 2356941, 2356952 and 2356943 contain the supplementary crystallographic data for this paper.[46a–c]

Acknowledgements

We thank SERB [CRG/2022/001499] for financial support. The DST-FIST facility is also partially acknowledged. SB acknowledges a CSIR-project-funded Senior Research Fellowship (SRF) and BITS-Pilani Hyderabad (India) for an Institute Research Fellowship. The Central Analytical Laboratory Facility of BITS-Pilani Hyderabad is greatly acknowledged. SB also partially acknowledges an Institute of Eminence (IoE)-IISc postdoctoral fellowship. MC Lab and ProFM Lab are greatly acknowledged for their research facilities and device fabrication capabilities, respectively. This work has been dedicated to SB's father, the late Subrata Kumar Bhuin.

References

1 J. L. B. Vázquez, Y. A. A. Sánchez, L. A. R. Cortés and B. R. Molina, Dual-State Emission (DSE) in Organic Fluorophores: Design and Applications, *Chem. Mater.*, 2021, **33**, 7160–7184.
2 T. Schembri, J. Albert, H. Hebling, V. Stepanenko, O. Anhalt, K. Shoyama, M. Stolte and F. Würthner, Supramolecular Engineering of Narrow Absorption Bands by Exciton Coupling in Pristine and Mixed Solid-State Dye Aggregates, *ACS Cent. Sci.*, 2025, **11**, 452–464.
3 Y. Sun, S. Xu, H. Hang, J. Xi, H. Dong, B. Jiao, G. Zhou and X. Yang, The third strategy: modulating emission colors of organic light-emitting diodes with UV light during the device fabrication process, *Chem. Sci.*, 2024, **15**, 8506–8513.
4 S. Bhuin, P. Sharma, P. Chakraborty, O. P. Kulkarni and M. Chakravarty, Solid-state emitting twisted π-conjugate as AIE-active DSE-gen: in vitro anticancer properties against FaDu and 4T1 with biocompatibility and bioimaging, *J. Mater. Chem. B*, 2023, **11**, 188–203.
5 A. Huber, J. Dubbert, T. D. Scherz and J. Voskuhl, Design Concepts for Solution and Solid-State Emitters – A Modern

Viewpoint on Classical and Non-Classical Approaches, *Chem. – Eur. J.*, 2023, **29**, e202202481.

6 Y. Xu, L. Ren, D. Dang, Y. Zhi, X. Wang and L. Meng, A Strategy of ''Self-Isolated Enhanced Emission'' to Achieve Highly Emissive Dual-State Emission for Organic Luminescent Materials, *Chem. – Eur. J.*, 2018, **24**, 10383–10389.

7 S. Bhuin, P. Chakraborty, P. Sivasakthi, P. K. Samanta and M. Chakravarty, Double-Site Twisted D-π-D′ Conjugates with Versatile Photophysical Facets for Diverse Optical Applications and Wash-Free Bioimaging of Cancer Cells, *ACS Appl. Opt. Mater.*, 2023, **1**, 1289–1300.

8 S. Bhuin, P. Chakraborty, P. Sivasakthi, P. K. Samanta, P. Yogeeswari and M. Chakravarty, Asymmetrical organic D–π–A conjugate with 'V'-shaped crystal packing: quest to transcend the limits of photophysical properties and application, *J. Mater. Chem. C*, 2023, **11**, 11270–11282.

9 F. Yu, H. Zhao, Y. Li, G. Xia and H. Wang, D–A-Type fluorophores with efficient dual-state emission for imaging at ultralow concentration, *Mater. Chem. Front.*, 2022, **6**, 155–162.

10 L. A. R. Cortes, F. J. Hernandez, M. Rodrıguez, R. A. Toscano, A. J. Sanchez, R. C. Otero and B. R. Molina, Conformational emissive states in dual-state emitters with benzotriazole acceptors, *Matter*, 2023, **6**, 1140–1159.

11 S. Riebe, S. Adam, B. Roy, I. Maisuls, C. G. Daniliuc, J. Dubbert, C. A. Strassert, I. Schapiro and J. Voskuhl, Bridged Aromatic Oxo- and Thioethers with Intense Emission in Solution and the Solid State, *Chem. – Asian J.*, 2021, **16**, 2307–2313.

12 J. Dubbert, M. Valtolina, A. Huber, T. D. Scherz, C. Wölper, C. G. Daniliuc, O. Filiba, S. Sen, I. Schapiro, F. Rizzo and J. Voskuhl, Tuning the Emission Behaviour of Halogenated Bridged Ethers in Solution, as Solids and as Aggregates by Chalcogen Substitution, *ChemPhotoChem*, 2023, **7**, e202200169.

13 M. Schmiedtchen, L. Höfmann, J. Balszuweit and J. Voskuhl, Small Molecular Dibenzochalcogenophenes as Potent Organic Emitters, *Chem. – Eur. J.*, 2025, **31**, e01977.

14 S. Bhuin, P. Chakraborty, P. Yogeeswari and M. Chakravarty, Twisted Molecular Core Conjugated Oxo-Ether as a Fluorescent Probe for Lipid-Droplets Bioimaging and Live Cancer Cell Discrimination, *ACS Appl. Bio Mater.*, 2025, **8**(4), 2985–3001.

15 M. Mandal, S. Mardanya, A. Saha, M. Singh, S. Ghosh, T. Chatterjee, R. Patra, S. Bhunia, S. Mandal, S. Mukherjee, R. Debnath, C. M. Reddy, M. Das and P. K. Mandal, Charge-transfer mediated J-aggregation in red emitting ultra-small-single-benzenic meta-fluorophore crystals, *Chem. Sci.*, 2025, **16**, 901–909.

16 C. A. Shen, D. Bialas, M. Hecht, V. Stepaneko, K. Sugiyasu and F. Würthner, Polymorphism in Squaraine Dye Aggregates by Self-Assembly Pathway Differentiation: Panchromatic Tubular Dye Nanorods versus J-Aggregate Nanosheets, *Angew. Chem., Int. Ed.*, 2021, **60**, 11949–11958.

17 J. Zhou, W. Zhang, X. F. Jiang, C. Wang, X. Zhou, B. Xu, L. Liu, Z. Xie and Y. Ma, Magic-Angle Stacking and Strong Intermolecular π–π Interaction in a Perylene Bisimide Crystal: An Approach for Efficient Near-Infrared (NIR) Emission and High Electron Mobility, *J. Phys. Chem. Lett.*, 2018, **9**, 596–600.

18 P. R. Das, A. Mazumder, M. Rajeevan, R. S. Swathi and M. Hariharan, Energy landscape of perylenediimide chromophoric aggregates, *Phys. Chem. Chem. Phys.*, 2024, **26**, 2007–2015.

19 S. Wu, W. Zhang, C. Li, Z. Ni, W. Chen, L. Gai, J. Tian, Z. Guo and H. Lu, Rational design of CT-coupled J-aggregation platform based on Aza-BODIPY for highly efficient phototherapy, *Chem. Sci.*, 2024, **15**, 5973–5979.

20 L. Krivosudsky and E. Rakovsky, Catena-Poly[[(pyrazine-2-carboxamide-κN^4)copper(I)]-μ_3-iodido], *Acta Crystallogr., Sect. E: Crystallogr. Commun.*, 2014, **E70**, m267–m268.

21 X. He, C. Chen, Z. Zhang, L. Wen, Y. Ma, Y. Cao and Y. Liu, π–π_{2max}: Bridging molecular characteristics to crystal packing in nitro-containing two-dimensional energetic materials, *Def. Technol.*, 2025, **49**, 192–202.

22 Y. Wei, R. Yang, G. Cui, S. Dai, G. Pan, J. Wang, H. Ren, W. Ma, Z. Gu, C. Zhang, G. Li, Z. Liu, B. Xu and W. Tian, Low-Pressure Sensitive Piezochromic Fluorescence Switching of Tetraphenylethylene-Anthraquinone, *Chem. – Eur. J.*, 2023, **29**, e202301070.

23 F. Glocklhofer, A. Petritz, E. Karner, M. J. Bojdys, B. Stadlober, J. Frohlich and M. M. Unterlass, Dicyano- and tetracyanopentacene: foundation of an intriguing new class of easy-to-synthesize organic semiconductors, *J. Mater. Chem. C*, 2017, **5**, 2603–2610.

24 Y. Wen, H. Liu, S. T. Zhang, G. Pan, Z. Yang, T. Lu, B. Li, J. Cao and B. Yang, Modulating Room Temperature Phosphorescence by Oxidation of Thianthrene to Achieve Pure Organic Single-Molecule White-Light Emission, *CCS Chem.*, 2021, **3**, 1940–1948.

25 N. J. Hestand and F. C. Spano, Expanded Theory of H- and J-Molecular Aggregates: The Effects of Vibronic Coupling and Intermolecular Charge Transfer, *Chem. Rev.*, 2018, **118**, 7069–7163.

26 A. Gavezzotti, Are Crystal Structures Predictable?, *Acc. Chem. Res.*, 1994, **27**(10), 309–314.

27 A. Gavezzotti and G. Fillippini, Geometry of the Intermolecular X-H—Y (X, Y = N, O) Hydrogen Bond and the Calibration of Empirical Hydrogen-Bond Potentials, *J. Phys. Chem.*, 1994, **98**, 4831–4837.

28 S. Ma, S. Du, G. Pan, S. Dai, B. Xu and W. Tian, Organic molecular aggregates: From aggregation structure to emission property, *Aggregate*, 2021, **2**, e96.

29 A. Tordo, E. Jeanneau, M. Bordy, Y. Bretonniere and J. Hasserodt, Crystal-packing modes determine the solid-state ESIPT fluorescence in highly dipolar 2′-hydroxychalcones, *J. Mater. Chem. C*, 2021, **9**, 12727–12731.

30 H. Piwonski, S. Nozue and S. Habuchi, The Pursuit of Short-wave Infrared-Emitting Nanoparticles with Bright Fluorescence through Molecular Design and Excited-State Engineering of Molecular Aggregates, *ACS Nanosci. Au*, 2022, **2**, 253–283.

31 G. W. Coates, A. R. Dunn, L. M. Henling, D. A. Dougherty and R. H. Grubbs, *Angew. Chem., Int. Ed. Engl.*, 1997, **36**,

248–251.32; S. Kumar, P. Tourneur, J. R. Adsetts, M. Y. Wong, P. Rajamalli, D. Chen, R. Lazzaroni, P. Viville, D. B. Cordes, A. M. Z. Slawin, Y. Olivier, J. Cornil, Z. Ding and E. Z. Colman, Photoluminescence and electrochemiluminescence of thermally activated delayed fluorescence (TADF) emitters containing diphenylphosphine chalcogenide-substituted carbazole donors, *J. Mater. Chem. C*, 2022, **10**, 4646–4667.

32 M. Zheng, Y. Li, Y. Wei, L. Chen, X. Zhou and S. Liu, Determining the Energy Gap between the S_1 and T_1 States of Thermally Activated Delayed Fluorescence Molecular Systems Using Transient Fluorescence Spectroscopy, *J. Phys. Chem. Lett.*, 2022, **13**, 2507–2515.

33 J. Yuan, Z. Xu and M. O. Wolf, Sulfur-bridged chromophores for photofunctional materials: using sulfur oxidation state to tune electronic and structural properties, *Chem. Sci.*, 2022, **13**, 5447–5464.

34 B. Li, L. Zhou, H. Cheng, Q. Huang, J. Lan, L. Zhou and J. You, Dual-emissive 2-(2′-hydroxyphenyl)oxazoles for high performance organic electroluminescent devices: discovery of a new equilibrium of excited state intramolecular proton transfer with a reverse intersystem crossing process, *Chem. Sci.*, 2018, **9**, 1213–1220.

35 W. Li, Y. Pan, L. Yao, H. Liu, S. Zhang, C. Wang, F. Shen, P. Lu, B. Yang and Y. Ma, A Hybridized Local and Charge-Transfer Excited State for Highly Efficient Fluorescent OLEDs: Molecular Design, Spectral Character, and Full Exciton Utilization, *Adv. Opt. Mater.*, 2014, **2**, 892–901.

36 Y. Zhang, B. He, J. Liu, S. Hu, L. Pan, Z. Zhao and B. Z. Tang, Aggregation-induced emission and the working mechanism of 1-benzoyl and 1-benzyl pyrene derivatives, *Phys. Chem. Chem. Phys.*, 2018, **20**, 9922–9929.

37 A. S. Velasco, O. A. Reyes, A. Kähäri, S. Lipinski, L. M. Cavinato, R. D. Costa, M. A. Kostiainen and E. A. Plaza, Controlling aggregation-induced emission by supramolecular interactions and colloidal stability in ionic emitters for light-emitting electrochemical cells, *Chem. Sci.*, 2024, **15**, 2755–2762.

38 Q. Wu, T. Zhang, Q. Peng, D. Wang and Z. Shuai, Aggregation induced blue-shifted emission – the molecular picture from a QM/MM study, *Phys. Chem. Chem. Phys.*, 2014, **16**, 5545–5552.

39 S. Bhuin, S. Bhattacharya and M. Chakravarty, Acceptor–donor–acceptor-linked triphenylamine and phenothiazine motifs as cousin molecules: the methyl effect on stimuli-responsiveness, crystallochromism, and dual-state emission, *New J. Chem.*, 2021, **45**, 21236–21247.

40 S. Bhuin, S. Halder, S. K. Saha and M. Chakravarty, Binding interactions and FRET between bovine serum albumin and various phenothiazine-/anthracene-based dyes: a structure–property relationship, *RSC Adv.*, 2021, **11**, 1679–1693.

41 Q. Peng, L. Yang, Y. Li, Y. Zhang, T. Li, Y. Qin, Y. Song, H. Hou and K. Li, Aggregation/Viscosity-Induced Emission and Third-Order Nonlinear Optical Signal Inversion in a TICT System, *J. Phys. Chem. C*, 2020, **124**(41), 22684–22691.

42 G. Haberhauer, Planarized and Twisted Intramolecular Charge Transfer: A Concept for Fluorophores Showing Two Independent Rotations in Excited State, *Chem. – Eur. J.*, 2017, **23**, 9288–9296.

43 L. Chen, Y. Feng, Y. Dang, C. Zhong and D. Chen, A deep-red emission fluorescent probe with long wavelength absorption for viscosity detection and live cell imaging, *Anal. Bioanal. Chem.*, 2020, **412**, 7819–7826.

44 N. Yadav, U. Deori, A. K. Manna and P. Rajamalli, Regulating Spatial Configuration in Donor-π-Acceptor for through-Space Exciton Transfer: Concentration-Independent Emitter for OLEDs, *Adv. Opt. Mater.*, 2025, **21**, 2402820.

45 S. Banerjee, P. Singh, P. Purkayastha and S. K. Ghosh, Evolution of Organic Light Emitting Diode (OLED) Materials and their Impact on Display Technology, *Chem. – Eur. J.*, 2025, **20**, e202401291.

46 (*a*) CCDC 2356941: Experimental Crystal Structure Determination, 2026, DOI: **10.5517/ccdc.csd.cc2k3lcn**; (*b*) CCDC 2356952: Experimental Crystal Structure Determination, 2026, DOI: **10.5517/ccdc.csd.cc2k3lq0**; (*c*) CCDC 2356943: Experimental Crystal Structure Determination, 2026, DOI: **10.5517/ccdc.csd.cc2k3lfq**.

